Research Square

Preprints are preliminary reports that have not undergone peer review.
They should not be considered conclusive, used to inform clinical practice,
or referenced by the media as validated information.

The rigid finite element method for fast fluid–structure interaction of slender bodies in OpenFOAM

Artem Nuriev

nuriev_an@mail.ru

Kazan Federal University

Boudkhil Affane

Kazan Federal University

A. Pozdeeva

Kazan Federal University

Research Article

Keywords: rigid finite element method, flexible multibody system, fluid–structure interaction, convergence, OpenFOAM, Turek–Hron benchmark

Posted Date: November 24th, 2026

DOI: https://doi.org/10.21203/rs.3.rs-11579073/v1

License: This work is licensed under a Creative Commons Attribution 4.0 International License.
Read Full License

Additional Declarations: No competing interests reported.

The rigid finite element method for fast fluid–structure interaction of slender bodies in OpenFOAM

A. Nuriev[1*], B. Affane[1] and A. Pozdeeva[1]

[1*]N. I. Lobachevsky Institute of Mathematics and Mechanics, Kazan Federal University, Kremlyovskaya str. 18, Kazan, 420008, Russia.

*Corresponding author(s). E-mail(s): nuriev_an@mail.ru;
Contributing authors: boudkhil.affane@gmail.com;
ssspozdeeva@gmail.com;

Abstract

For fluid–structure interaction (FSI) of slender flexible bodies, we propose a structural model in the form of a chain of rigid segments with distributed inertia connected by elastic hinges (a model of the rigid finite element type). We show that, with an appropriate representation of the clamp, the chain is a consistent second-order discretisation of the Euler–Bernoulli (Rayleigh) beam, and that second order is retained for large deflections. The model is embedded in the standard multibody solver of OpenFOAM and requires no external code, no second mesh and no interface interpolation; geometric nonlinearity is accounted for automatically. The implementation is verified on the Turek–Hron benchmark. The deflections and frequencies in the structural tests differ from the reference by at most 1.6% (axial displacements by up to 3.4%), and the frequencies in FSI2 and FSI3 differ from refined reference solutions by at most 1.5% and 0.2%, respectively. An analysis of the error sources shows that the discretisation error of the chain is small compared with the errors of the one-dimensional idealisation and of the flow computation. At comparable accuracy, the FSI computation with the proposed model is 3–6 times faster than with the finite-volume solid solver `solids4foam`.

Keywords: rigid finite element method, flexible multibody system, fluid–structure interaction, convergence, OpenFOAM, Turek–Hron benchmark

1 Introduction

Fluid–structure interaction of slender flexible bodies – flags, fins, flapping wings, plant leaves and stems, flexible sensors – underlies a wide range of natural and engineered systems. In the design of bio-inspired propulsors and devices with elastic elements, the coupled problem has to be solved many times while the stiffness, mass distribution and kinematics are varied. In such computations the structural model has to meet three requirements at once: it must be accurate enough not to introduce an error comparable with that of the flow computation; it must be cheap compared with the flow computation itself; and it must be easy to embed in an existing CFD code without separate infrastructure. These requirements determine the content of this work.

The most general approach couples the flow equations with the equations of continuum elasticity. In commercial software it is implemented either within a single program, as in COMSOL Multiphysics and STAR-CCM+, or by co-simulation of a CFD code and a finite-element code, for example ANSYS Fluent with ANSYS Mechanical or STAR-CCM+ with Abaqus. A similar approach is available in free software as well, for example in OpenFOAM, the most widely used open-source CFD toolbox. In its ecosystem the coupled problem is solved by the finite-volume solid solver `solids4foam` [1, 2]; another route is to couple the flow solver with an external finite-element or multibody code through a coupling library such as preCICE [3], or through a dedicated interface, as in the coupling of OpenFOAM with the MBDyn code [4, 5]; flexible multibody formulations have also been coupled with flow solvers [6, 7]. These approaches provide the stress field and handle bodies of arbitrary shape, but they require a separate structural mesh and interpolation at the interface, and for a slender body the thickness has to be resolved as well. Yet a slender body deforms mainly in bending, and a one-dimensional rod model is sufficient for it. Geometrically exact models have been developed for such rods [8, 9], together with their discretisations as multibody systems [10] and as discrete elastic rods [11]; a review of flexible multibody approaches is given in [12]. The question is how to discretise this rod so that the model is accurate, cheap and easy to embed at the same time.

One of the simplest discretisations is a chain of rigid links connected by elastic hinges. Replacing an elastic structure by rigid bodies with elastic connections is a classical idea, and several well-known classes of models are based on it: the Hencky bar-chain [13–15], the rigid finite element method [16–18], pseudo-rigid-body models [19, 20] and impedance-based lumped-parameter models [21, 22]. In the Hencky bar-chain (HBM) the beam is replaced by rigid bars with rotational springs of stiffness EI/a; Wang, Zhang, Challamel and co-authors established its equivalence to central finite differences, obtained exact buckling and vibration solutions, including elastically restrained ends, and constructed a nonlocal continualisation [14, 15]. In the HBM the mass is usually lumped at the hinges. The rigid finite element method (RFEM) uses rigid elements that carry the inertia and massless spring–damping elements, and it has been developed for large displacements. The model studied here can be assigned to this type: it is the planar modified formulation of the RFEM [17, Ch. 4], in which the hinge rotations serve as generalised coordinates. In pseudo-rigid-body models the hinge parameters are fitted to the response of compliant links, and in impedance-based lumped-parameter models to the boundary impedance.

In FSI, chains of rigid bodies have been used to describe the chordwise flexibility of flapping wings [23], insect wings coupled with the unsteady vortex-lattice method [24], and bio-inspired swimming robots [25]. Arranz et al. [26] coupled an immersed-boundary flow solver with a multibody dynamics library and represented a three-dimensional flag by 25 rigid plates connected by torsional springs. In all these works the chain serves as a convenient engineering model: the number of links and the hinge stiffnesses are chosen by common sense, and the question of what the solution converges to, and how fast, as the chain is refined is not raised. Moreover, the loads on the links are often obtained from simplified flow models – the vortex-lattice method or characteristics averaged over each link – so that the error of the structural model is not separated from that of the aerodynamics. Hence the widespread view of such models as crude. For example, Zhang et al. [7], who coupled a finite-volume flow solver with the multibody code MBDyn through radial-basis-function interpolation and verified the approach on the Turek–Hron benchmark, model the flexible parts by nonlinear shear-deformable beam elements and write that chains of rigid bodies connected by springs [24], "by neglecting structural flexibility entirely", cannot capture the influence of elastic deformation on the load distribution.

We show that this view is not necessary. The work is built around three ideas.

The first idea is embeddability. A chain of rigid bodies fits naturally into the multibody solvers that CFD toolboxes already contain for floating and moving bodies. In OpenFOAM, the `rigidBodyDynamics` library implements recursive algorithms for tree-structured systems of bodies connected by joints [27] and is linked to the mesh-motion solver, which passes fluid forces to the bodies and body motion to the mesh. If a flexible body is represented by a chain of such bodies, an FSI computation needs neither an external code nor a second mesh nor interface interpolation. There is only one obstacle: the standard restraints of the library act between a body and the fixed frame and cannot model a hinge between neighbouring bodies. We show that it is removed by a single small class acting in joint space.

The second idea is consistency. For the chain to be a discretisation of an elastic rod rather than an imitation of it, its limit and order of convergence must be known. For the variant with *distributed* inertia, in which mass and rotary inertia belong to the segments (this is precisely the variant that corresponds to a rigid-body system in a CFD code), the mass matrix and the continuum limit have not, to our knowledge, been written in closed form, and the order of convergence and its dependence on the clamp treatment have not been studied. We show that second order is governed by the representation of the clamp (similar end-spring corrections are known for the HBM [14]) and find the condition for second order for a division into equal segments; it is dual to the primary division of the RFEM with half-length end elements.

The third idea is geometric nonlinearity at no extra cost. The multibody solver integrates the exact nonlinear equations of motion of the chain: joint rotations are finite, and centrifugal and Coriolis forces are included automatically. A chain embedded in such a solver is therefore immediately suitable for large deflections, whereas beam finite elements require a dedicated geometrically nonlinear formulation. The natural question is whether the second-order convergence established for the linear problem is retained in the nonlinear regime.

Testing these ideas requires a full flow computation, in which the fluid forces are integrated over the actual surface of each segment, and a test case in which the structural model operates in a coupled problem with large deflections and a strong added-mass effect and for which reliable reference solutions exist. The Turek–Hron benchmark [28] is such a test. However, a plain comparison with the reference says little about the model: the difference combines the errors of the fluid mesh, the time step, the coupling scheme, the number of segments and, finally, the one-dimensional idealisation itself. We therefore separate these sources by dedicated computations.

Accordingly, the contributions of this work are as follows: (i) the nonlinear equations of motion of the chain with distributed inertia, the closed-form mass matrix of the linearised problem and the limiting integro-differential problem are derived, from which the Euler–Bernoulli (Rayleigh) equation and all cantilever boundary conditions follow; (ii) it is proved that a clamp hinge of stiffness $2EI/\Delta x$ provides second-order convergence, the relation of this division to the primary division of the RFEM is established, and it is shown numerically that second order is retained for large static and dynamic deflections; (iii) the chain is embedded in the standard multibody library of OpenFOAM by a single joint-space restraint, and practical rules for its use are formulated; (iv) the approach is verified on the structural and FSI tests of Turek and Hron with separation of the error sources, and the computational cost is compared with that of a finite-volume solid solver.

The paper is organised as follows. Section 2 presents the nonlinear equations of the chain and their linearisation. Section 3 derives the continuum limit, examines the clamp condition and discusses the nonlinear limit and damping. Section 4 verifies convergence numerically for small and large deflections. Section 5 describes the embedding of the chain in OpenFOAM (implementation details are given in Appendix A), and Section 6 presents the Turek–Hron tests and the error analysis. Section 7 discusses the place of the model among other approaches, its limitations and extensions.

2 The rigid-segment chain

Since the multibody solver in which the chain will be embedded integrates the exact equations of motion, we first derive these equations and then linearise them for the convergence analysis.

2.1 Kinematics and equations of motion

A cantilever of length L, bending stiffness EI and mass per unit length ρA is divided into N rigid segments of length $\Delta x = L/N$ (Fig. 1). Segment i has mass $m = \rho A\,\Delta x$ and moment of inertia about its centre of mass $I_{\mathrm{cm}} = m\Delta x^2/12$; for a beam of thickness h, the rotary inertia of the cross-section $mh^2/12$ is added. The segments are connected by elastic hinges of stiffness $k_\theta = EI/\Delta x$, and the first segment is attached to the support by a hinge of stiffness k_0, whose choice is discussed in Sect. 3.2.

The degrees of freedom are the absolute angles φ_i, $i = 1, \dots, N$, of the segments with respect to the undeformed axis; the angle φ_i is naturally associated with the segment centre $\xi_i = (i - \frac{1}{2})\Delta x$. The clamp prescribes the support angle $\varphi_0 = 0$. We stress that only the section $x = 0$ is fixed: the first segment rotates, and the rotation

$\varphi_1 - \varphi_0$ in the clamp hinge is nonzero. The relative hinge angles $\theta_i = \varphi_i - \varphi_{i-1}$ are related to the absolute ones by $\boldsymbol{\varphi} = \mathbf{S}\boldsymbol{\theta}$, where $\mathbf{S}$ is the lower-triangular matrix of ones. It is the relative angles that serve as joint coordinates in the multibody solver (Sect. 5).

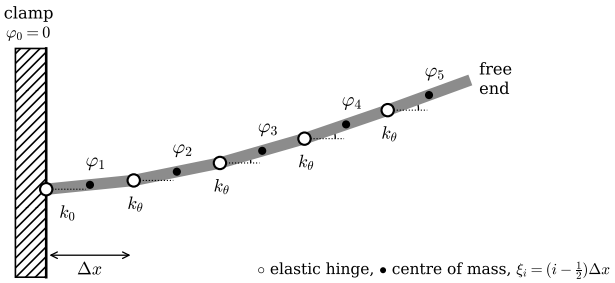

Fig. 1 Rigid-segment model of a cantilever ($N = 5$). The hinges are located at $x = j\Delta x$, $j = 0, \ldots, N-1$; the clamp hinge has stiffness k_0

Let $\mathbf{e}(\varphi) = (\cos\varphi, \sin\varphi)$. The centre of mass of segment i is located at

$$\mathbf{r}_i = \sum_{k=1}^{N} a_{ik}\, \mathbf{e}(\varphi_k), \qquad a_{ik} = \begin{cases} \Delta x, & k < i, \\ \Delta x/2, & k = i, \\ 0, & k > i, \end{cases} \tag{1}$$

and the hinge located at $j\Delta x$ on the undeformed axis is at $\sum_{k\le j} \Delta x\, \mathbf{e}(\varphi_k)$. The kinetic energy of the segments (by König's theorem) and the potential energy of the hinges are

$$T = \frac{1}{2}\sum_{i=1}^{N} m\,|\dot{\mathbf{r}}_i|^2 + \frac{1}{2}\sum_{i=1}^{N} I_{\mathrm{cm}}\dot{\varphi}_i^2, \qquad U = \frac{1}{2}k_0\varphi_1^2 + \frac{1}{2}\sum_{i=2}^{N} k_\theta(\varphi_i - \varphi_{i-1})^2. \tag{2}$$

Since $\dot{\mathbf{r}}_i = \sum_k a_{ik}\dot{\varphi}_k\, \mathbf{e}'(\varphi_k)$ and $\mathbf{e}'(\varphi_j)\cdot\mathbf{e}'(\varphi_k) = \cos(\varphi_j - \varphi_k)$, the kinetic energy takes the form

$$T = \frac{1}{2}\sum_{j,k} \big[A_{jk}\cos(\varphi_j - \varphi_k) + \delta_{jk} I_{\mathrm{cm}}\big]\dot{\varphi}_j\dot{\varphi}_k, \qquad A_{jk} = m\sum_i a_{ij}a_{ik}, \tag{3}$$

and Lagrange's equations give

$$\sum_k \big[A_{jk}\cos(\varphi_j - \varphi_k) + \delta_{jk} I_{\mathrm{cm}}\big]\ddot{\varphi}_k + \sum_k A_{jk}\sin(\varphi_j - \varphi_k)\,\dot{\varphi}_k^2 = -\frac{\partial U}{\partial \varphi_j} + Q_j, \tag{4}$$

where Q_j are the generalised external forces (gravity, fluid forces). Equations (4) are exact for arbitrary rotations; it is these equations, written in the joint coordinates θ_i, that the multibody solver integrates.

2.2 Linearised problem

For the convergence analysis, consider small vibrations about the straight configuration. For small angles $\cos(\varphi_j - \varphi_k) \approx 1$, the terms with $\dot\varphi_k^2$ are of second order, and equations (4) without external forces become $\mathbf{M}\ddot{\mathbf{q}} + \mathbf{K}\mathbf{q} = \mathbf{0}$ with $\mathbf{q} = [\varphi_1, \dots, \varphi_N]^\mathsf{T}$. The deflections of the centres of mass and of the hinges in this approximation are

$$y_i^{\mathrm{cm}} = \sum_k a_{ik}\varphi_k = \sum_{k=1}^{i-1} \varphi_k \Delta x + \varphi_i \frac{\Delta x}{2}, \qquad y(j\Delta x) = \sum_{k=1}^{j} \varphi_k \Delta x. \tag{5}$$

The stiffness matrix is tridiagonal,

$$\mathbf{K} = k_\theta \begin{bmatrix} 1 + k_0/k_\theta & -1 & & & \\ -1 & 2 & -1 & & \\ & \ddots & \ddots & \ddots & \\ & & -1 & 1 \end{bmatrix}, \tag{6}$$

and the substitution $\boldsymbol{\varphi} = \mathbf{S}\boldsymbol{\theta}$ makes it diagonal, $\mathbf{S}^\mathsf{T}\mathbf{K}\mathbf{S} = \mathrm{diag}(k_0, k_\theta, \dots, k_\theta)$, without changing the eigenvalues. After summation in A_{jk}, the mass matrix $\mathbf{M} = \mathbf{A} + I_{\mathrm{cm}}\mathbf{E}$ takes the closed form

$$M_{ij} = \rho A\, \Delta x^3 \Big[N - \max(i,j) + \tfrac{1}{2}\Big] - \delta_{ij} \frac{\rho A\, \Delta x^3}{6} = \rho A\, \Delta x^2 \big[L - \max(\xi_i, \xi_j)\big] - \delta_{ij} \frac{\rho A\, \Delta x^3}{6}. \tag{7}$$

The first term corresponds to the translation of the centres of mass, and the diagonal correction to the rotary inertia and the finite segment length. The matrix $\mathbf{M}$ is symmetric, positive definite and full.

For segments of different lengths Δx_i, the hinge between segments $i-1$ and i must have stiffness $k_i = 2EI/(\Delta x_{i-1} + \Delta x_i)$, i.e. EI divided by the distance between the segment centres; the clamp hinge corresponds to $\Delta x_{-1} = 0$, in agreement with the result of Sect. 3.2.

3 Continuum limit and the clamp condition

3.1 Limiting problem

For the interior rows, $(\mathbf{K}\boldsymbol{\varphi})_i = -EI\, \Delta x\, (\varphi_{i+1} - 2\varphi_i + \varphi_{i-1})/\Delta x^2$, i.e. the stiffness matrix coincides with the central-difference approximation of the second derivative at the segment centres. The boundary rows take the same form if ghost values are introduced at the centres of ghost segments $\xi_0 = -\Delta x/2$ and $\xi_{N+1} = L + \Delta x/2$:

$$\tilde\varphi_0 = -\Big(\frac{k_0}{k_\theta} - 1\Big)\varphi_1, \qquad \tilde\varphi_{N+1} = \varphi_N. \tag{8}$$

Setting $\varphi_i = \varphi(\xi_i, t)$ and expanding in Taylor series, we obtain

$$(\mathbf{K}\boldsymbol{\varphi})_i = -EI\,\Delta x\left[\varphi''(\xi_i) + O(\Delta x^2)\right]. \tag{9}$$

The sum $\sum_j [L - \max(\xi_i, \xi_j)]\,\ddot{\varphi}_j\,\Delta x$ in $(\mathbf{M}\ddot{\boldsymbol{\varphi}})_i$ is the composite midpoint rule; the kink of the kernel at $\xi = \xi_i$ falls on a quadrature node, and the diagonal correction in (7) is of relative order Δx^2. Hence

$$(\mathbf{M}\ddot{\boldsymbol{\varphi}})_i = \rho A\,\Delta x\left[\int_0^L [L - \max(\xi_i, \xi)]\,\ddot{\varphi}(\xi, t)\,d\xi + O(\Delta x^2)\right]. \tag{10}$$

Dividing by Δx, we obtain the integro-differential equation

$$EI\,\varphi''(x,t) = \rho A\int_0^L [L - \max(x,\xi)]\,\ddot{\varphi}(\xi,t)\,d\xi, \qquad \varphi(0,t) = 0, \quad \varphi'(L,t) = 0. \tag{11}$$

The kernel $G(x,\xi) = L - \max(x,\xi)$ is the Green's function of the operator $-\partial^2/\partial x^2$ with the conditions $G_x(0,\xi) = 0$, $G(L,\xi) = 0$, so that both operators in the eigenvalue problem $-EI\varphi'' = \omega^2\rho A\,G\varphi$ are positive definite. Differentiating (11) by Leibniz's rule gives $EI\varphi''' = -\rho A\int_0^x \ddot{\varphi}\,d\xi$. In the limit, the hinge deflections (5) become $y(x,t) = \int_0^x \varphi\,d\xi$, so that $\varphi = y'$, $y(0,t) = 0$ and $\int_0^x \ddot{\varphi}\,d\xi = \ddot{y}$. Thus

$$EI\,\frac{\partial^4 y}{\partial x^4} + \rho A\,\frac{\partial^2 y}{\partial t^2} = 0, \tag{12}$$

and none of the four cantilever boundary conditions is imposed; all of them follow from the limit: $y(0) = 0$ by construction; $y'(0) = \varphi(0) = 0$ from the clamp row of $\mathbf{K}$; $y''(L) = \varphi'(L) = 0$ from the last row; and $y'''(L) = \varphi''(L) = 0$ from (11) at $x = L$, where the kernel vanishes. If the rotary inertia of the cross-section is kept in I_{cm}, the limit is the Rayleigh beam.

3.2 The clamp condition

It follows from (8) that the clamp stiffness determines where the condition $\varphi = 0$ is effectively imposed. For $k_0 = 2k_\theta$ we obtain $\tilde{\varphi}_0 = -\varphi_1$, i.e. $\frac{1}{2}(\tilde{\varphi}_0 + \varphi_1) = 0$. Since the points ξ_0 and ξ_1 are symmetric about $x = 0$, this approximates the condition $\varphi(0) = 0$ to second order. An energy argument gives the same result. A hinge between the centres of neighbouring segments approximates the bending energy of a portion of length Δx, whereas the clamp hinge is responsible for the portion $[0, \xi_1]$ of length $\Delta x/2$, on which $\varphi' \approx 2\varphi_1/\Delta x$; its energy is $\frac{1}{2}EI(2\varphi_1/\Delta x)^2(\Delta x/2) = \frac{1}{2}(2EI/\Delta x)\varphi_1^2$, whence $k_0 = 2EI/\Delta x$. The free end needs no correction: $\tilde{\varphi}_{N+1} = \varphi_N$ is symmetric about $x = L$ and approximates $\varphi'(L) = 0$ to second order.

Thus, for $k_0 = 2EI/\Delta x$ both operators together with the boundary conditions are approximated to $O(\Delta x^2)$, and standard perturbation estimates for the generalised eigenvalue problem give an eigenvalue error of $O(\Delta x^2)$.

The chain is closely related to the primary division of the RFEM [17, Sects. 3.1, 6.1], in which the roles of segments and hinges are interchanged: hinges of stiffness $EI/\Delta x$ are placed at the midpoints of N parts of length Δx, the rigid half element at the clamp is fixed, and the last element has half length. The angles are then associated with the nodes $x_j = j\Delta x$ rather than with segment centres; the condition $\varphi(0) = 0$ holds exactly at the node $x_0 = 0$, and the half-length end element gives a second-order approximation of $\varphi'(L) = 0$. Thus the chain with $k_0 = 2EI/\Delta x$ and the primary division of the RFEM are two dual second-order discretisations, with the angles at cell centres and at nodes, respectively.

3.3 Nonlinear limit

The analysis above concerns the linearised problem, whereas the multibody solver integrates the nonlinear equations (4). Let us see what the nonlinear chain tends to. The positions (1) of the centres of mass and hinges are midpoint rules for the integrals $\int \mathbf{e}(\theta(s))\,ds$, and the hinge energy $\frac{1}{2}\sum k_\theta(\varphi_i - \varphi_{i-1})^2 = \frac{1}{2}\sum EI\,\Delta x\,[(\varphi_i - \varphi_{i-1})/\Delta x]^2$ is a difference approximation of the integral $\frac{1}{2}\int EI\,\theta'^2\,ds$. Therefore the Lagrangian of the chain approximates the Lagrangian of the inextensible geometrically exact Euler–Bernoulli rod [8] (with rotary inertia of the cross-section, the Rayleigh rod)

$$\mathcal{L} = \frac{1}{2}\int_0^L \left(\rho A\,|\dot{\mathbf{r}}|^2 + \rho I\,\dot\theta^2\right) ds - \frac{1}{2}\int_0^L EI\,\theta'^2\,ds, \qquad \mathbf{r}'(s) = \mathbf{e}(\theta(s)), \tag{13}$$

where s is the arc length and $\theta(s)$ the tangent angle. The same arguments as in the linear case show that for $k_0 = 2EI/\Delta x$ this approximation is of second order, including the clamp condition. A rigorous convergence proof for the nonlinear problem is beyond the scope of this work; instead, second order is verified numerically for large static and dynamic deflections in Sect. 4.2. Note that the limit of the nonlinear chain is precisely a one-dimensional inextensible rod. Shear, extension and two-dimensional effects near the clamp are absent from it, and their contribution is a separate model error that does not decrease with N.

3.4 Damping in the hinges

The model naturally admits viscous damping in the hinges. If the damping coefficients are proportional to the stiffnesses, $c_i = \eta k_i$, the linearised equations acquire the term $\mathbf{C}\dot{\mathbf{q}}$ with $\mathbf{C} = \eta\mathbf{K}$. The limit for $\mathbf{C}$ repeats that for $\mathbf{K}$: $(\mathbf{C}\dot{\boldsymbol\varphi})_i = -\eta EI\,\Delta x\,[\dot\varphi''(\xi_i) + O(\Delta x^2)]$, and the limit is a beam with Kelvin–Voigt internal friction

$$EI\,\frac{\partial^4 y}{\partial x^4} + \eta EI\,\frac{\partial^5 y}{\partial x^4 \partial t} + \rho A\,\frac{\partial^2 y}{\partial t^2} = 0. \tag{14}$$

Since the damping is stiffness-proportional, the mode shapes do not change, and the modal damping ratios are $\zeta_n = \eta\omega_n/2$, i.e. they grow with the mode number. For example, for the cantilever with $L = 1$ m, $EI = 1000$ N m^2 and $\rho A = 1$ kg/m, whose frequencies are given in Sect. 4, the value $\eta = 10^{-3}$ s gives $\zeta_1 = 0.056$ and $\zeta_3 = 0.97$:

the first mode is lightly damped, and the third is almost critically damped. This also determines the choice of η. If the Kelvin–Voigt parameter of the material is known, it is used directly; if the damping serves to suppress unresolved high modes, it is convenient to prescribe the admissible damping ζ^* of the highest resolved mode n^* and to set $\eta = 2\zeta^*/\omega_{n^*}$. Strong damping of high modes tightens the stability limit of explicit integration schemes, $\Delta t \le 2(\sqrt{1+\zeta_{\max}^2} - \zeta_{\max})/\omega_{\max}$ with $\zeta_{\max} = \eta\omega_{\max}/2$; implicit schemes, in particular the Newmark scheme used in Sect. 6, have no such limit, and damping of unresolved modes acts as a useful filter. No damping is used in the Turek–Hron tests, as in the reference.

4 Numerical verification of convergence

We now verify the conclusions of Sect. 3 numerically: first for small vibrations, where the exact solution is known, and then for large deflections, where second order is predicted but not proved.

4.1 Small vibrations

The natural frequencies of a cantilever with $L = 1$ m, $EI = 1000$ N m^2 and $\rho A = 1$ kg/m were computed for $N = 3$–200 and compared with the Euler–Bernoulli values $f_n = (\beta_n L)^2\sqrt{EI/\rho A}\,/(2\pi L^2)$, i.e. 17.696, 110.898 and 310.517 Hz for the first three modes. For $k_0 = 2EI/\Delta x$ all discrete frequencies lie below the continuum ones and converge to them monotonically (Fig. 2a). The observed orders are $p = 2.00$, 1.99, 1.99 for modes 1–3 at $N = 10$–100, and the errors of the mode shapes at the hinges converge with $p \approx 1.97$. The error grows quickly with the mode number: at $N = 50$ the errors of the first three frequencies are in the ratio $1 : 3.5 : 5.7$. It is more convenient to characterise the required resolution by the smallest number of segments that provides a given accuracy (Table 1): an accuracy of 1% requires $N \gtrsim 4n$–$7n$ segments for mode n, and 0.1% requires $N \gtrsim 14n$–$22n$. The mode shapes for $N = 10$ are shown in Fig. 3.

Table 1 Smallest number of segments N for which $|\varepsilon_f|$ does not exceed a given value ($k_0 = 2EI/\Delta x$)

Accuracy	mode 1	mode 2	mode 3	mode 4	mode 5
1%	7	13	17	20	22
0.1%	22	40	52	61	69

The effect of the clamp treatment is shown in Fig. 2b and Table 2, where a second-order finite-difference (FD) scheme for $EIy'''' + \rho A\ddot{y} = 0$ with the same number of unknowns is included for comparison (five-point stencil, ghost points $y_{-1} = y_1$ at the clamp and $y'' = y''' = 0$ at the free end). Two common simplifications are also shown – equal stiffness of all hinges and a fixed first segment; they converge only to first order, with errors close to $\mp 1/N$. For $k_0 = 2EI/\Delta x$ the convergence is of second order, and the accuracy is 1.8 (mode 1) to 3.5 (mode 3) times higher than that of the FD scheme.

The primary division of the RFEM also converges to second order, with errors of opposite sign and half as large; our computation for it reproduces the data of the monograph [17, Table 6.2] for the modified formulation (with ten spring–damping elements, 0.23, 0.80 and 1.30% for the first three modes, against 0.23, 0.79 and 1.29%). We use equal segments, since then all bodies and boundary patches are identical and the elastic part starts exactly at the attachment point. The difference in accuracy is small on the scale of the FSI problem: at $N = 20$ the error of the second mode is -0.40% for the chain and $+0.20\%$ for the RFEM division, whereas the one-dimensional idealisation of the Turek–Hron flag accounts for 1.2% in this mode (Sect. 6.6).

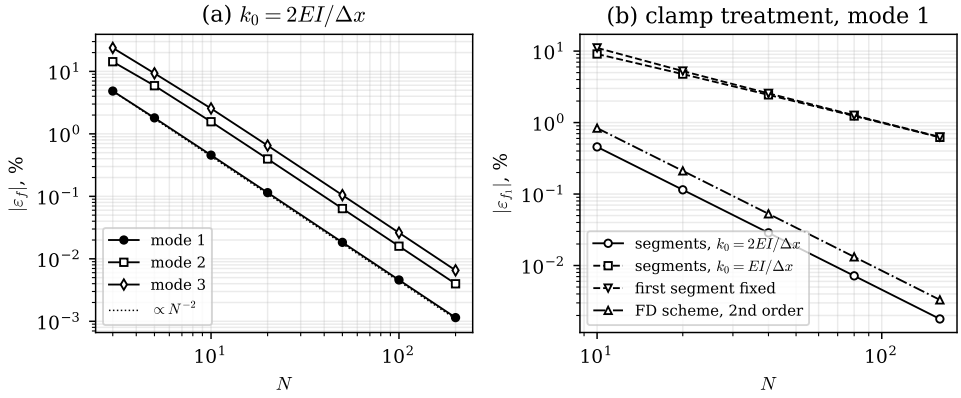

Fig. 2 Relative frequency error versus the number of segments: (a) first three modes, $k_0 = 2EI/\Delta x$; (b) first mode for different clamp treatments and for the second-order finite-difference scheme

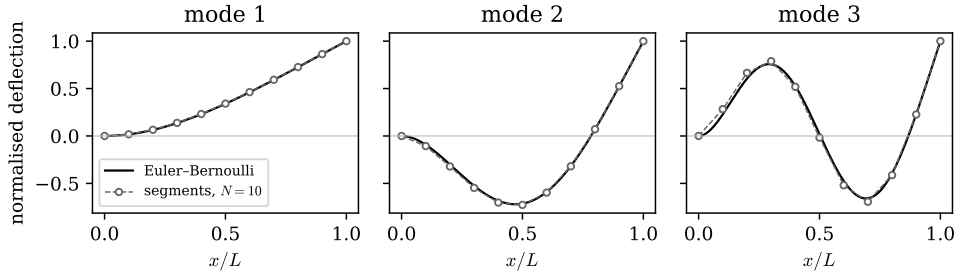

Fig. 3 Mode shapes of the rigid-segment model ($N = 10$, deflections at the hinges) and of the Euler–Bernoulli cantilever. The shapes are normalised to unit tip deflection. The kink at the clamp reflects the rotation of the first segment in the clamp hinge

Table 2 Relative frequency error ε_f (%) for different clamp treatments and for the second-order finite-difference (FD) scheme

N	$k_0 = 2EI/\Delta x$		$k_0 = EI/\Delta x$		first segment fixed		FD, 2nd order	
	mode 1	mode 3	mode 1	mode 3	mode 1	mode 3	mode 1	mode 3
10	−0.457	−2.55	−9.11	−8.23	+11.09	+12.39	−0.837	−8.26
20	−0.115	−0.650	−4.77	−4.52	+5.26	+5.56	−0.211	−2.21
40	−0.0287	−0.163	−2.44	−2.38	+2.56	+2.63	−0.0528	−0.563
80	−0.0072	−0.0409	−1.23	−1.22	+1.27	+1.28	−0.0132	−0.141
160	−0.0018	−0.0102	−0.621	−0.617	+0.629	+0.633	−0.0033	−0.0354
p	2	2	1	1	1	1	2	2

4.2 Large deflections

To verify the nonlinear limit (Sect. 3.3), equations (4) were solved directly: static equilibria were found by minimising the potential energy followed by Newton iterations, and the dynamics was integrated by an eighth-order Runge–Kutta method with a relative tolerance of 10^{-11}.

The test object is a cantilever under its own weight: length $L = 0.351$ m, thickness $h = 0.02$ m, density $\rho_s = 1000$ kg/m^3, Poisson's ratio $\nu = 0.4$, bending stiffness per unit width $EI = Eh^3/[12(1-\nu^2)]$; the segment inertia includes the rotary inertia of the cross-section, $I_{\mathrm{cm}} = m(\Delta x^2 + h^2)/12$. Three static cases with increasing deflection are considered:

- S1: $E = 5.6$ MPa, $g = 2$ m/s^2;
- S2: $E = 1.4$ MPa, $g = 2$ m/s^2;
- S3: $E = 1.4$ MPa, $g = 20$ m/s^2.

The exact static reference is the equilibrium of the inextensible rod under the distributed vertical load $q = \rho_s h g$ – the elastica

$$EI\,\theta''(s) = q\,(L-s)\cos\theta(s), \qquad \theta(0) = 0, \quad \theta'(L) = 0, \tag{15}$$

solved by collocation to a tolerance of 10^{-12}. The tip rotations are 3.7°, 14.5° and 71.6° at $|u_y|/L = 0.05$, 0.19 and 0.79. As Fig. 4a shows, in all three cases the error converges with order 2.00, and its constant is almost independent of the deflection: at $N = 20$ the error of u_y is 0.25%, 0.24% and 0.19%, and that of u_x is 0.35%, 0.34% and 0.16%.

In the dynamic case D, the cantilever of case S2 is released from rest with gravity switched on and then oscillates between the undeformed position and a tip deflection of about $0.37L$. No independent continuum solution exists for this case, so convergence was assessed from the sequence of computations with $N = 5$–160: the time of the first lowest position and the tip deflection at that instant were recorded. The observed orders from successive differences are 1.85–2.03 for the displacements and 1.8–2.6 for the time. Relative to the Richardson extrapolation from $N = 80$ and 160 (Fig. 4b), the errors at $N = 20$ are 0.30% in time and 0.25% in deflection – the same as for small amplitudes.

Thus second-order convergence is retained for large static and dynamic deflections, and the error constant is practically independent of the amplitude. We stress that this is convergence to the nonlinear one-dimensional rod; its difference from the actual elastic body is estimated separately in Sect. 6.6. Cases S2, S1 and D coincide with the structural tests CSM1, CSM2 and CSM3 of the Turek–Hron benchmark [28], whose reference solutions were obtained for a two-dimensional elastic body; the comparison with them is given in Sect. 6.3.

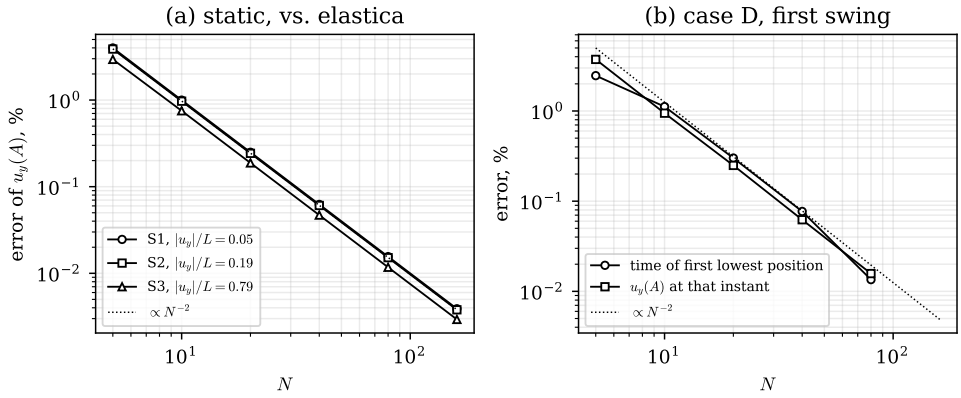

Fig. 4 Convergence for large deflections, nonlinear chain with $k_0 = 2EI/\Delta x$: (a) static tip deflection under self-weight compared with the elastica, cases S1–S3 with tip rotations of 3.7°, 14.5° and 71.6°; (b) case D – cantilever released from rest under gravity, time and tip deflection at the first lowest position, error relative to the Richardson extrapolation from $N = 80$ and 160

5 Embedding the chain in OpenFOAM

We now turn to the first idea – implementing the chain in a standard multibody solver. In OpenFOAM, this uses the `rigidBodyDynamics` library and the associated mesh-motion solver `rigidBodyMotion`. Each segment is defined as a rigid body with mass m_i, moment of inertia $I_{\mathrm{cm},i}$ and centre of mass at the segment midpoint; its parent is the previous segment (for the first segment, the support), and its joint is revolute (`Rz`), with the relative angle θ_i as the joint coordinate. Each segment is associated with a boundary patch of its surface: the motion solver integrates the fluid forces over this patch, applies them to the body and moves the patch with the body, deforming the interior mesh. The library computes the kinetic energy from the body data, and it coincides with (2); the equations of motion are solved exactly by Featherstone's recursive algorithm [27], i.e. in the form (4). The third idea – geometric nonlinearity – is thus realised automatically.

The only missing element is the elastic hinge between bodies. The restraints available in the library act on a single body with respect to the fixed frame: the moment is proportional to the absolute angle φ_i rather than the relative one, no reaction is

applied to the neighbouring body, and the damping depends on the absolute angular velocity. Applied to a chain, they model not a beam but a beam on an elastic rotational foundation. A correct hinge is obtained if the moment is applied not as an external force on the body but as a generalised joint force. The restraint interface of the library allows this: in addition to external forces, it accumulates generalised joint forces, which the forward-dynamics algorithm uses as joint torques. For an `Rz` joint,

$$\tau_i = -k_i(\theta_i - \theta_i^0) - c_i\dot{\theta}_i \tag{16}$$

is the internal moment in the hinge: it acts on body i and, with the opposite sign, on its parent, and the damping depends on the relative angular velocity. The new restraint `linearJointSpring`, which implements (16), has about 90 lines of code, of which the moment computation itself takes five. It is compiled into a small user library and loaded at run time, so that neither OpenFOAM nor the flow solver is modified. A nonzero angle $\theta_i^0(t)$ prescribes an initial curvature and can serve as a simple model of active actuation.

Setting up a computation reduces to a mesh in which the surface of the flexible body is split into one patch per segment, and to a dictionary of bodies and hinges, which is written by a short script from L, EI, ρA, h and N. Several rules following from Sects. 2 and 3 must be observed: the first segment must be a moving body with a clamp hinge $k_0 = 2EI/\Delta x_0$; the segment inertia must include the rotary inertia of the cross-section; and the solver parameter `accelerationDamping` must equal 1, since otherwise all inertias are effectively scaled. The correspondence between model quantities and dictionary entries, a dictionary fragment, the restraint code and the full list of practical rules are given in Appendix A.

6 Turek–Hron benchmark

6.1 Problem statement and flag model

The benchmark [28] considers a channel of length 2.5 m and height $H = 0.41$ m with a rigid cylinder of radius $R = 0.05$ m centred at $(0.2, 0.2)$ and an elastic flag of thickness $h = 0.02$ m attached to it, whose free end is at the point $A = (0.6, 0.2)$. A parabolic inflow profile with mean velocity $\bar{U}$ is ramped up as $(1 - \cos(\pi t/2))/2$ for $t < 2$ s; the fluid has $\rho_f = 1000$ kg/m^3 and $\nu_f = 10^{-3}$ m^2/s, and the flag material has $\nu_s = 0.4$. In FSI2, $\rho_s = 10^4$ kg/m^3, $E = 1.4$ MPa, $\bar{U} = 1$ m/s; in FSI3, $\rho_s = 10^3$ kg/m^3, $E = 5.6$ MPa, $\bar{U} = 2$ m/s. The benchmark also includes the structural tests CSM1–CSM3 (flag under gravity without flow) and the tests CFD1–CFD3 with a rigid flag. The outputs are the displacements of point A and the drag and lift on the cylinder and flag per unit width; periodic signals are characterised by the mean $= (\max + \min)/2$, the amplitude $= (\max - \min)/2$ and the frequency.

The accuracy is characterised by the relative difference $\varepsilon_q = (q - q_{\mathrm{ref}})/|q_{\mathrm{ref}}|$, computed separately for each quantity q – the mean, amplitude and frequency of each signal; the means of u_y and lift, which are small compared with the amplitudes, are not used for this. Unless stated otherwise, the reference is [28] for the structural tests, the refined monolithic solution [29] for FSI2 and the high-order solution [30] for FSI3.

The aggregate accuracy figures in the abstract and conclusions are not averages: for the structural tests they are the largest $|\varepsilon_q|$ over the displacements and frequencies of Table 4, for FSI2 the deviation of the u_y frequency (for the frequencies of u_x and u_y on meshes M1–M3 it is 1.4–1.6%, Table 5), and for FSI3 the largest $|\varepsilon_q|$ over the frequencies f_1, f_2 on mesh M3 (Table 6).

The flag is modelled by a chain of $N = 20$ segments ($N = 30$ in some computations). Three decisions matter in passing from the two-dimensional elastic body to a rod. The clamp is placed at the intersection of the flag with the circle, $x_r = 0.2 + (R^2 - h^2/4)^{1/2} = 0.24899$ m, so that $L = 0.35101$ m. Since the reference flag is a two-dimensional body, the bending stiffness is taken for plane strain, $EI = Eh^3/[12(1-\nu_s^2)]$, which is 19% larger than $Eh^3/12$; with the plane-stress stiffness all frequencies would be 8% lower. Finally, the segment inertia includes the rotary inertia of the cross-section, $I_{\mathrm{cm}} = m(\Delta x^2 + h^2)/12$, which is comparable with the segment's own inertia for $h/\Delta x \approx 1$.

The dry natural frequencies of the flag (Rayleigh rod, plane strain) are 0.338, 2.11 and 5.88 Hz for FSI2 and 2.14, 13.4 and 37.2 Hz for FSI3. The FSI2 oscillations at about 2 Hz are close to the second dry mode, and according to Table 1, $N = 20$ resolves the second mode to about 0.4%.

6.2 Meshes and numerical parameters

The flow is computed with the `pimpleFoam` solver of OpenFOAM v2112 (implicit second-order `backward` scheme in time, `linearUpwind` for convection) on block-structured meshes generated with `blockMesh`. All meshes have the same topology (Fig. 5). The cylinder is surrounded by an O-grid in the rectangle $0.063 \le x \le x_b$, $0.063 \le y \le 0.337$, whose right boundary $x_b = x_r + 5\Delta x$ coincides with the end of the fifth segment. The flag has finite thickness and is cut out of the mesh; along it the cells are uniform with spacing $h_f = \Delta x/n_s$, where n_s is the number of cells per segment, so that segment boundaries coincide with mesh faces and each segment forms a separate boundary patch. Above and below the flag the mesh is refined towards its surface, where the wall-normal cell size is about $1.2\,h_f$. In the O-grid the spacing along the cylinder circumference is about $1.2\,h_f$ (smaller near the flag root), and the radial spacing is constant at about $1.6\,h_f$. In the outer blocks the spacing is about $2.2\,h_f$, and up to $4.5\,h_f$ along the sides of the O-block; in the wake behind the flag the cells grow geometrically to about $20\,h_f$ at the outlet. All sizes expressed in h_f are the same on all meshes, i.e. the meshes are geometrically similar. The depth of the domain is 1 m, so forces and segment masses are per unit width.

The resolution is thus set by a single parameter n_s. Four meshes are used (Table 3): three meshes M1–M3 for $N = 20$, forming a sequence with spacing reduced by factors of 1.34 and 1.50, and mesh M4 for $N = 30$, whose spacing along the flag is close to that of M2.

The interior mesh points are moved by solving a Laplace equation for the displacement with diffusivity $1/r$ [31], where r is the distance to the cylinder and flag. This makes the cells next to each segment move almost rigidly with it and transfers the deformation to larger cells further away. The fluid–structure coupling is partitioned: the bodies and the mesh are updated at every outer PIMPLE iteration with

Table 3 Computational meshes: N is the number of segments, n_s the number of cells per segment along the flag, h_f the spacing along the flag

Mesh	N	n_s	h_f, mm	cells around cylinder	total cells	Used in
M1	20	6	2.93	115	18 860	FSI2, FSI3
M2	20	8	2.19	154	34 012	FSI2, FSI3, CFD2, CFD3
M3	20	12	1.46	227	76 206	FSI2, FSI3, CFD3
M4	30	6	1.95	171	41 807	FSI2 ($N = 30$)

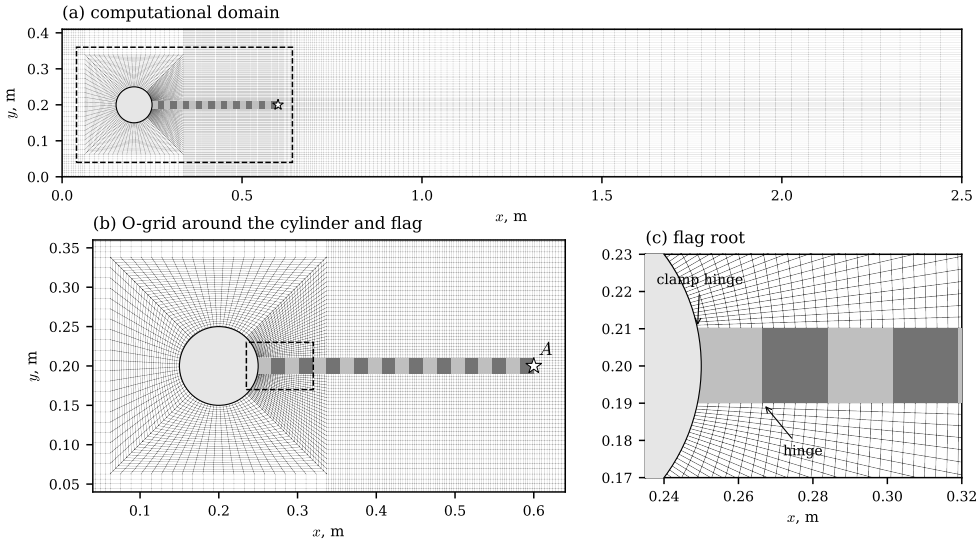

Fig. 5 Mesh M1: (a) computational domain; (b) O-grid around the cylinder and flag, with segments shown in alternating shades (each is a separate boundary patch), the star marks point A; (c) flag root with the clamp hinge on the cylinder surface and the first interior hinge. Meshes M2–M4 have the same topology

relaxation of the body accelerations. The required coupling strength is determined by the ratio of the added mass to the flag mass; with the added mass of a rigid plate $\rho_f \pi L^2/4 \approx 97$ kg/m, this ratio is about 1.4 in FSI2 and 14 in FSI3. FSI2 used a time step $\Delta t = 10^{-3}$ s, 6 outer iterations and a relaxation factor of 0.5; FSI3 used $\Delta t = 5 \cdot 10^{-4}$ s, 12 iterations and a relaxation factor of 0.1, consistent with the convergence estimate of the iterations $\omega \lesssim 2/(1 + m_a/m) \approx 0.13$; the instability of partitioned schemes at large added mass and the role of relaxation in the coupling iterations are discussed in [32–34]. The structure is integrated with the Newmark scheme with $\gamma = 0.5$, $\beta = 0.25$, without numerical dissipation. The displacement of point A is taken from the mesh node at the end of the last segment, and the forces are integrated over the cylinder and all segment patches. The regime is considered periodic when successive maxima of u_y change by less than 1% over 5–6 periods.

One geometric feature should be noted. At a hinge, the rigid outlines of neighbouring segments separate on the convex side and overlap by $(h/2)\Delta\theta$ on the concave side. In the mesh this causes neither a gap nor self-intersection: there is a single node at the junction, shared by the faces of both segments, and the mismatch is absorbed

by one adjacent face. Since $(h/2)\Delta\theta = (h/2)\kappa\Delta x = \varepsilon\Delta x$, where ε is the strain of the outer fibre, this mismatch is the elongation (shortening) of the surface fibres of the bent beam concentrated at the hinge; in FSI2 it amounts to fractions of a millimetre.

6.3 Structural tests

As noted in Sect. 4.2, tests CSM1–CSM3 coincide with cases S2, S1 and D; the results for $N = 20$ are compared with the reference in Table 4. The displacements and frequencies differ from the reference by 0.6–1.6%, except for the mean and amplitude of the small axial displacement u_x in CSM3 (3.4%), whereas with the plane-stress stiffness the deflection in CSM1 would be -78.3 mm, i.e. 18% larger. The comparison with the elastica splits the difference into two parts. The converged one-dimensional solution deflects more than the two-dimensional reference body: by 0.37% in u_y and 0.85% in u_x in CSM1, and by 0.45% and 0.94% in CSM2; the discretisation at $N = 20$ adds another 0.25% and 0.35%. Zhang et al. [7] obtained the same small excess of the static deflection with 20 shear-deformable beam elements ($u_y = -17.08$ mm in CSM2). The residual difference is therefore mainly due to the one-dimensional idealisation and the clamp position; we return to this question in Sect. 6.6.

Table 4 Structural tests: displacement of point A (mm); CSM3: mean ± amplitude [frequency, Hz]; $N = 20$, plane strain

Test		Present	Reference [28]	Difference
CSM1	u_x	-7.273	-7.187	1.2%
	u_y	-66.51	-66.10	0.6%
CSM2	u_x	-0.475	-0.469	1.3%
	u_y	-17.09	-16.97	0.7%
CSM3	u_x	-14.79 ± 14.79 [1.093]	-14.305 ± 14.305 [1.0995]	3.4% / 0.6%
	u_y	-64.26 ± 66.20 [1.092]	-63.607 ± 65.160 [1.0995]	1.6% / 0.7%

6.4 FSI2

The flag oscillations start growing at about $t = 5$ s and become periodic by $t \approx 9$ s (Fig. 6); the statistics are taken over the last 2 s of a 15 s run. The results on meshes M1–M3 are given in Table 5. Between meshes M2 and M3 the frequencies change by at most 0.1%, the amplitudes by at most 0.5% and the mean drag by 0.2%, i.e. the solution is converged in the fluid mesh to about 0.5%.

The converged solution is naturally compared not with the original reference values [28] but with the refined monolithic solution [29] obtained on the finest mesh with $\Delta t = 5 \cdot 10^{-4}$ s. Relative to it, the mean drag is 1.1% higher, the drag amplitude 1.6% lower, the amplitudes of u_y and lift 3.1% and 4.5% higher, and the frequencies 1.4–1.6% higher. The mean u_x is a second-order quantity: for an inextensible flag $u_x \approx -\frac{1}{2}\int_0^L \varphi^2\,dx$ is proportional to the square of the bending amplitude, so the excess of the u_y amplitude alone accounts for about 6% of the 14% difference. The means of u_y and lift are small compared with the amplitudes and uninformative. In

Table 5 FSI2: mean ± amplitude and frequency f on meshes M1–M3 ($N = 20$, $\Delta t = 10^{-3}$ s); displacements in mm, forces in N/m

	M1	M2	M3	Reference [28]	Reference [29]
u_x	-16.73 ± 13.24	-16.88 ± 13.36	-16.95 ± 13.42	-14.58 ± 12.44	-14.85 ± 12.70
f, Hz	3.922	3.919	3.917	3.86	3.86
u_y	1.31 ± 83.72	1.30 ± 84.08	1.29 ± 84.22	1.23 ± 80.6	1.30 ± 81.7
f, Hz	1.960	1.960	1.958	1.93	1.93
drag	217.96 ± 75.19	217.75 ± 76.07	217.33 ± 76.43	208.83 ± 73.75	215.06 ± 77.65
f, Hz	3.917	3.917	3.915	3.86	3.86
lift	1.38 ± 249.11	1.38 ± 249.22	1.38 ± 248.47	0.88 ± 234.2	0.61 ± 237.8
f, Hz	1.960	1.960	1.960	1.93	1.93

the nondimensional quantities of Zhang et al. [7], also used in [35] (amplitude scaled by the cylinder diameter $d = 0.1$ m, $\mathrm{St} = fd/\bar{U}$, $C_d = F_D/(\frac{1}{2}\rho_f \bar{U}^2 d)$), the present solution gives $A/d = 0.84$, $\mathrm{St} = 0.196$ and $C_d = 4.35$; their beam finite-element approach gives 0.80, 0.19 and 4.18, with reference values quoted there of 0.83, 0.19 and 4.16 (in [7] d is called the radius, but the tabulated values correspond to $d = 0.1$ m). The instantaneous velocity magnitude in the periodic regime is shown in Fig. 7a: the flag bends in a shape close to the second dry mode, and a vortex street forms behind it. The origin of the remaining differences is analysed in Sect. 6.6.

6.5 FSI3

FSI3 is the most difficult case for a partitioned coupling, since the added mass is about 14 times the flag mass. With the coupling parameters given above, the computations on meshes M1–M3 are stable over the whole interval up to $t = 10$ s (Fig. 8); the oscillations start growing at about $t = 3.3$ s and become periodic by $t \approx 4.5$ s, and the statistics are taken over the last 2 s, i.e. about 11 periods of u_y; the instantaneous velocity field is shown in Fig. 7b.

The original FSI3 reference values [28] differ noticeably from later, more accurate results. Table 6 therefore also compares the present solution with the range of results of different solvers from [36], with the refined monolithic solution [29], with a monolithic finite-element solution on a sequence of meshes [37] and with a high-order solution with 525 thousand degrees of freedom [30]. On all three meshes the means, amplitudes and frequencies lie within the range of [36]. Under mesh refinement the mean drag decreases monotonically (478.5, 471.6 and 465.6 N/m) with an observed order of about 1.3; the extrapolation from the three meshes gives 456.6 N/m, and assuming second order on the two finest meshes gives 460.6 N/m, so the refined values of 460.3–460.5 N/m lie within this interval. The frequencies converge quickly, to 10.975 and 5.485 Hz, which is 0.2% and 0.1% above the high-order solution [30] and 0.4% and 0.5% above the refined monolithic solution [29]. On mesh M3 the displacement amplitudes differ from [30] by -0.4% (u_x) and 1.4% (u_y), the force amplitudes by 1.3% (drag) and 2.9% (lift), and the mean drag by 1.1%; relative to [29] these differences are 0.4% and 2.0%, 1.0% and 5.0%, and 1.1%, respectively. Unlike the other quantities, the lift amplitude increases under refinement and converges to about 163 N/m, remaining within the range of [36]; since in the rigid-flag test it decreases towards the reference instead (Sect. 6.6), this growth is related to the flag motion rather than to the mesh. Thus the apparent 25%

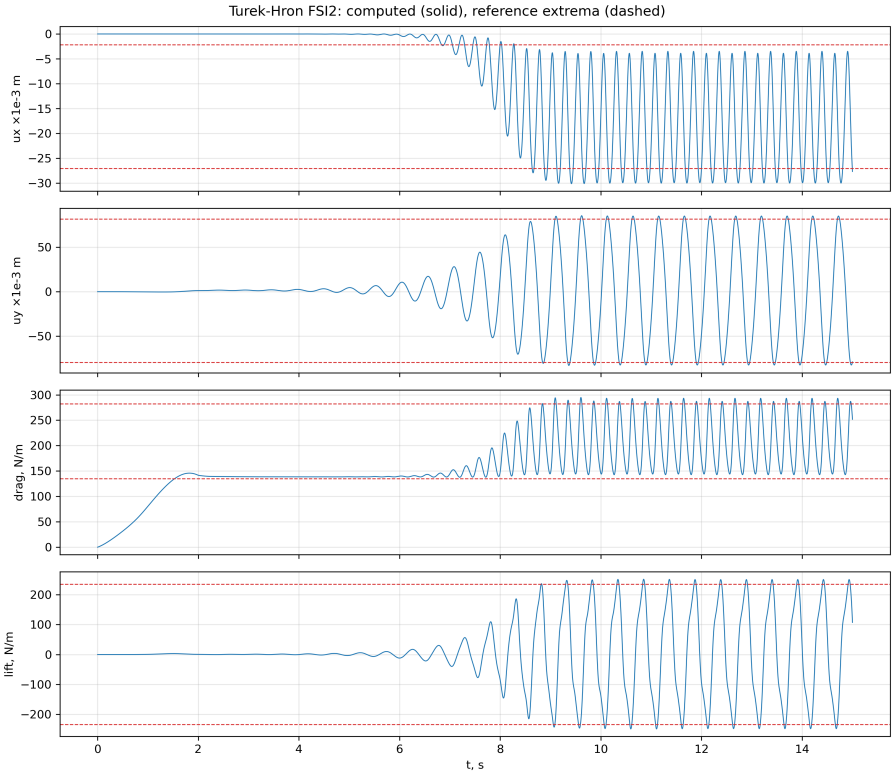

Fig. 6 FSI2: displacement of point A, drag and lift (solid lines) and the range of the reference values [28] (dashed); $N = 20$, mesh M1

difference of the drag amplitude from the original reference [28] is due to that reference itself. In the quantities of [7], the present solution gives $A/d = 0.36$, St $= 0.274$ and $C_d = 2.33$, against 0.35, 0.28 and 2.30 there.

Table 6 FSI3: comparison with other solvers; f_1 and f_2 are the frequencies of u_x and u_y

		Turek, Hron [28]	Solvers of [36][1]	Turek et al. [29][2]	Lozovskiy et al. [37]	Liu [30]	Present M1	Present M2	Present M3
u_x, mm	mean	−2.69	−3.04 ... −2.84	−2.88	−3.0	−2.91	−3.01	−2.98	−2.95
	ampl.	2.53	2.67 ... 2.87	2.72	2.9	2.74	2.78	2.76	2.73
u_y, mm	mean	1.48	1.28 ... 1.55	1.47	1.4	1.46	1.58	1.55	1.49
	ampl.	34.38	34.61 ... 36.63	34.99	36.1	35.2	35.97	35.89	35.70
Drag, N/m	mean	457.3	452.4 ... 474.9	460.5	458.0	460.3	478.5	471.6	465.6
	ampl.	22.66	26.19 ... 31.30	27.74	27.6	27.67	27.58	27.97	28.03
Lift, N/m	mean	2.22	1.81 ... 3.86	2.50	3.0	2.41	2.74	2.65	2.47
	ampl.	149.78	152.7 ... 165.9	153.91	154.5	157	155.4	159.1	161.6
f_1, Hz		10.9	10.84 ... 11.63	10.93	10.81	10.95	10.93	10.96	10.97
f_2, Hz		5.46	4.98 ... 5.51	5.46	5.40	5.48	5.47	5.48	5.48

[1] Minimum and maximum over the finest results of methods 1, 2b, 3, 5 and 7 of [36]; methods 2a, 4 and 6, which are far from mesh convergence or do not report forces, are excluded.

[2] Finest mesh, $\Delta t = 2.5 \cdot 10^{-4}$ s.

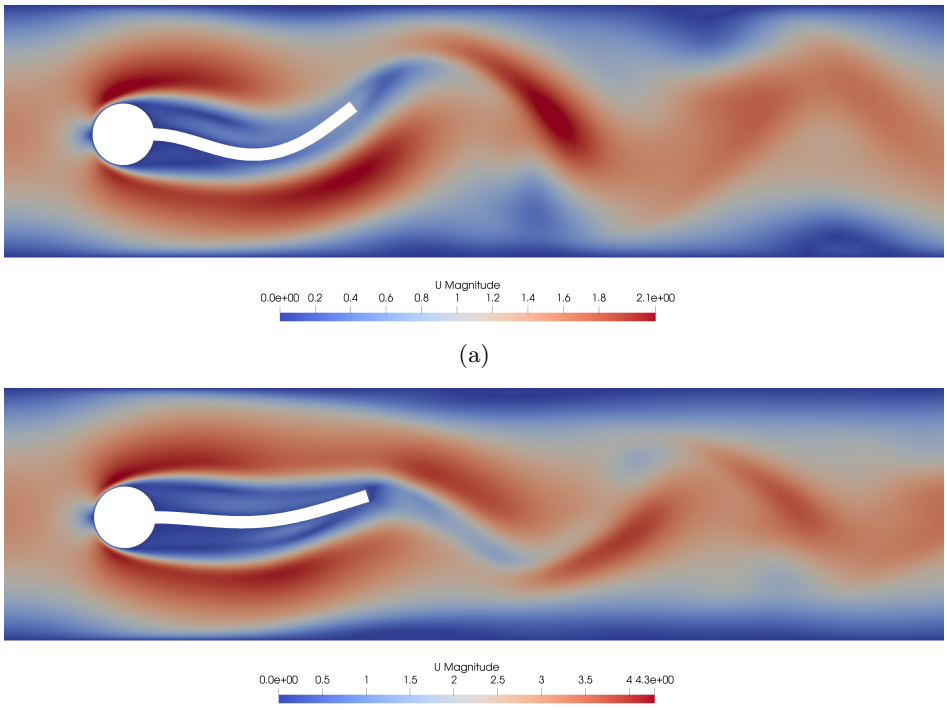

Fig. 7 Instantaneous velocity magnitude (m/s) in the periodic regime: (a) FSI2, $t = 9.2$ s; (b) FSI3, $t = 5.4$ s; $N = 20$

6.6 Sources of the remaining differences

Thus, in FSI3 the solution is at the level of the refined references, whereas in FSI2 systematic differences remain: the frequency is 1.5% higher, and the amplitudes and mean drag are 1–4% higher. To determine which of these belong to the rigid-segment model and which to other parts of the computation, the sources of the differences were separated by additional computations. Each of them isolates one possible source: the time step and coupling scheme, the number of segments, the flow discretisation, and the one-dimensional idealisation of the flag.

Table 7 FSI2: effect of the number of segments, time step and coupling parameters; relative changes of the statistics

Change	f	u_y amplitude	mean drag	lift amplitude
$N = 20 \to 30$ (meshes M2 $\to$ M4)	+0.26%	+0.7%	+1.1%	+1.2%
expected from the second dry mode	+0.22%			
$N = 30$: $\Delta t/2$, relaxation 0.3, 12 iterations	0	−0.05%	−0.04%	−0.17%

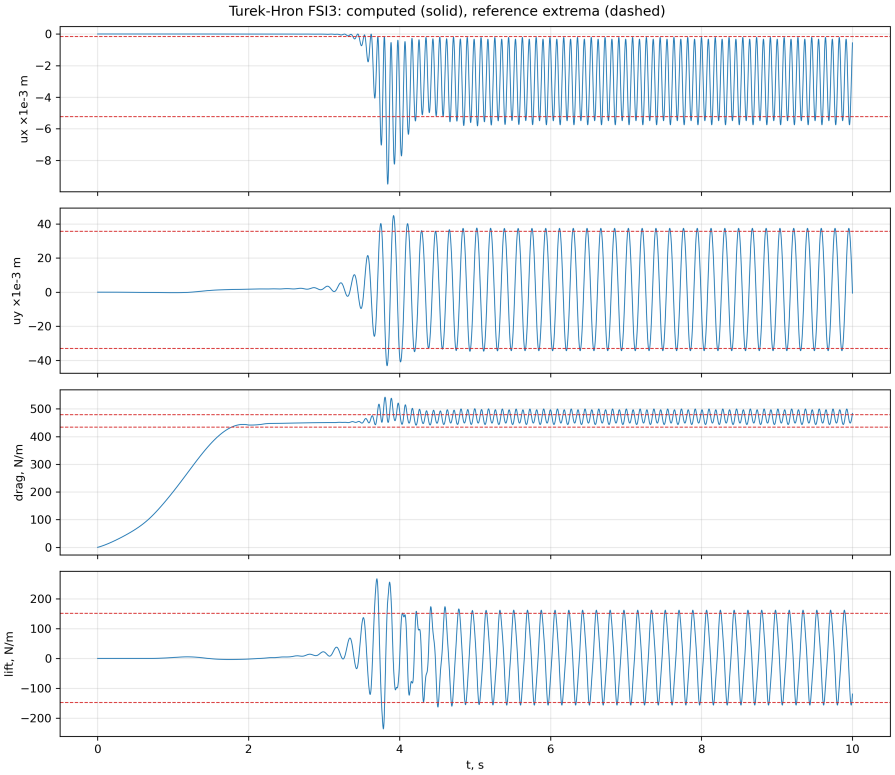

Fig. 8 FSI3: displacement of point A, drag and lift (solid lines) and the range of the reference values [28] (dashed); $N = 20$, mesh M2

Time step and coupling scheme.

The FSI2 computation with $N = 30$ on mesh M4 was repeated with half the time step, a relaxation factor of 0.3 instead of 0.5 and 12 outer iterations instead of 6. All statistics changed by less than 0.2%, and the frequency did not change (Table 7). Hence the time integration and the partitioned coupling are converged and are not a source of the differences.

Number of segments.

Increasing N from 20 to 30 raised the FSI2 frequency by 0.26%. The discretisation errors of the second dry mode of the flag are -0.39% at $N = 20$ and -0.18% at $N = 30$, which predicts an increase of 0.22%. The convergence of the chain established in Sect. 4 thus carries over to the coupled problem, and increasing N moves the frequency away from the reference rather than towards it. The amplitudes and mean drag increased by 0.7–1.2%; with second-order convergence this means that at $N = 20$ these quantities are converged in N to about 1–2%. The spacing of mesh M4 along the flag (1.95 mm) is close to that of mesh M2 (2.19 mm), and according to Table 5 the contribution of the fluid mesh to these changes is much smaller than observed.

Table 8 Rigid-flag tests CFD2 and CFD3 [28] on meshes M2 and M3; forces in N/m, deviation from the reference in parentheses. The extrapolation assumes second-order convergence and a spacing ratio of 1.5

	Mesh	drag	lift	f, Hz
CFD2	M2	137.64 (+0.7%)	10.65 (+1.1%)	–
	reference	136.7	10.53	–
CFD3	M2	451.38 ± 6.86 (+2.7%)	-9.08 ± 472.8 (+8.0%)	4.417 (+0.5%)
	M3	445.11 ± 6.29 (+1.3%)	-12.89 ± 455.2 (+4.0%)	4.431 (+0.8%)
	extrapolation	440.1 (+0.15%)	amplitude 441 (+0.8%)	
	reference	439.45 ± 5.62	-11.89 ± 437.8	4.396

Flow discretisation.

To separate the error of the flow computation from the structural model, the benchmark tests with a rigid, fixed flag were computed on the same meshes: CFD2 with the inflow velocity of FSI2 and CFD3 with that of FSI3 (Table 8).

- *CFD3 and FSI3.* For the rigid flag, the mean drag exceeds the reference by 2.7% on mesh M2 and by 1.3% on mesh M3. These values practically coincide with the excess of FSI3 over the refined monolithic solution [29] on the same meshes, 2.4% and 1.1%. Hence the drag excess in FSI3 is a property of the flow solution on the given mesh rather than of the structural model. Extrapolation assuming second-order convergence gives 440.1 N/m for CFD3, 0.15% above the reference, and for FSI3, as noted above, the interval 456.6–460.6 N/m, which contains the refined values.
- *CFD2 and FSI2.* On mesh M2 the rigid flag overestimates the drag by 0.7%, whereas FSI2 on the same mesh does so by 1.25%. Thus about half of the drag excess in FSI2 is due to the fluid mesh, and the other half is related to the flag motion: the u_y amplitude exceeds the reference by about 3%, and the mean drag grows with the amplitude.

The CFD3 frequency exceeds the reference by 0.5–0.8% and increases slightly under mesh refinement, so the flow computation may contribute up to 1% to the frequency differences in the FSI tests. Zhang et al. [7] obtained similar differences with another finite-volume solver: on meshes of 46 and 120 thousand cells, the mean CFD3 drag exceeds the reference by 0.95% and 0.66%, and the frequency by 1.2–1.5%.

Table 9 Dry natural frequencies of the FSI2 flag (Hz): two-dimensional finite-element model of the elastic flag in plane strain, clamped along the cylinder arc (biquadratic elements, mesh convergence 0.01%), and the rigid-segment chain for $N \to \infty$. The ratios are independent of E and ρ_s and are the same for FSI3

	mode 1	mode 2	mode 3
two-dimensional elastic flag (FEM)	0.3390	2.0866	5.687
rigid-segment chain, $N \to \infty$	0.3383	2.1123	5.879
difference	−0.2%	+1.2%	+3.4%

One-dimensional idealisation.

The last source is the model itself: the chain converges to a one-dimensional rod (Sect. 3.3), whereas the reference flag is a two-dimensional elastic body of relative thickness $h/L = 0.057$ clamped along the cylinder arc. This difference was estimated by computing the dry modes of the two-dimensional flag with plane-strain finite elements (Table 9). The rod is 1.2% stiffer in the second mode and 3.4% in the third, while its first mode is 0.2% softer, consistent with the 0.6% lower frequency in CSM3 (Table 4). These differences combine two effects: shear compliance alone lowers the frequencies of a Timoshenko cantilever by 0.25%, 1.7% and 3.9%, whereas attaching the flag along the curved cylinder surface stiffens the root and partly compensates for this. The FSI2 oscillations are close to the second dry mode (1.96 against 2.09–2.11 Hz). If the frequency of the coupled oscillations followed the frequency of this mode, the one-dimensional idealisation would account for up to 1.2% of the excess; since the FSI2 oscillations are a coupled self-excited mode whose frequency is partly set by the flow, the actual contribution is probably smaller, and 1.2% should be regarded as an upper bound. Together with the contribution of the flow computation (0.5–0.8% from the CFD3 test) and the accuracy of the reference frequency, given to two digits (±0.26%), this is consistent with the observed 1.5% at $N = 20$ and about 2% for $N \to \infty$. In FSI3 the added mass is about 14 times the flag mass, and the oscillation frequency of 5.48 Hz is far from the second dry mode at 13.4 Hz; the role of the stiffness is even smaller here, which is consistent with the agreement of the frequencies obtained in FSI3.

The excess of the FSI2 amplitudes (by 3–4.5%) is not quantitatively explained by these estimates. Possible causes are the difference in stiffness between the model and the two-dimensional flag, the extensibility of the flag, which is absent from the model, or features of the flow computation near the moving surface; separating them requires further computations.

To summarise: the computations are converged in the time step and coupling scheme and, to about 1–2%, in the number of segments. The drag differences are explained by the flow discretisation and decrease under mesh refinement. The FSI2 frequency difference consists of the contributions of the beam idealisation of the flag (at most 1.2%) and of the flow computation (0.5–0.8%); the former would be removed by a chain with shear, discussed in the next section. The 3–4.5% excess of the FSI2 amplitudes remains unexplained.

7 Discussion

Place of the model among other approaches.

Table 10 compares the rigid-segment chain with two approaches commonly used in OpenFOAM for FSI of slender bodies. Finite-element and multibody beam models coupled with the flow solver through preCICE, a dedicated interface or radial-basis-function interpolation [3, 5, 7] provide stresses and handle arbitrary geometry, but require a second code, a structural mesh, interface interpolation and a geometrically nonlinear formulation for large deflections; as Zhang et al. [7] note, the global interface interpolation becomes the main cost for large multibody systems. A finite-volume

solid solver such as `solids4foam` [1, 2] is consistent with the CFD code, but for a slender body it needs a mesh that resolves the thickness, which makes the structural computation much more expensive than for a system with $N \sim 20$–50 unknowns. The rigid-segment chain uses only standard OpenFOAM components, is geometrically exact for the inextensible rod and has no shear degrees of freedom, so shear locking cannot occur. It is also more accurate than related discretisations: the Hencky bar-chain with lumped masses is equivalent to central finite differences [15], and the chain with distributed inertia and $k_0 = 2EI/\Delta x$ is 1.8–3.5 times more accurate than the second-order scheme with the same number of unknowns (Table 2). Apart from implementation details, the results of this work carry over to the dual primary division of the RFEM.

Table 10 Qualitative comparison of structural models for FSI of slender bodies in OpenFOAM

	FE code via a coupling library	FV solid solver (`solids4foam`)	Rigid-segment chain
Additional software	structural code, coupling library	solid solver within OpenFOAM	one restraint class
Structural mesh	yes	yes, resolving the thickness	no (one patch per segment)
Interface data transfer	interpolation between meshes	conforming or interpolated	forces and moments on patches
Large deflections	nonlinear formulation	nonlinear formulation	built in (inextensible elastica)
Structural unknowns	10^2–10^4	10^3–10^5	$N \sim 20$–50
Stresses	full field	full field	hinge moments
Shear locking	possible for low-order elements	possible on coarse meshes	absent
Scope	arbitrary bodies	arbitrary bodies	tree-structured slender bodies

Cost.

The structural problem has $N = 20$ degrees of freedom, and its cost is negligible compared with the flow computation. This is seen directly from the run times: on mesh M2, one outer coupling iteration takes the same time in FSI2 and FSI3 (0.12 s on 8 processes), so the cost of a time step is proportional to the number of coupling iterations and is determined by the flow computation and mesh motion.

To compare the chain with an approach in which the flag is computed as a two-dimensional elastic body, two FSI2 computations were performed on the same machine (Intel Core i5-12450H, 2 MPI processes) (Table 11): a `solids4foam` [1, 2] computation following the developers' tutorial and verification script on their 2x mesh (partitioned coupling accelerated by IQN-ILS [38]), and our computation on mesh M1 with the same time step. The fluid meshes are similar in size, and the accuracy is comparable: the frequencies exceed the reference by 1.5 and 1.8%, and the other deviations of both computations are a few percent. With the same time step $\Delta t = 5 \cdot 10^{-4}$ s, a time step of the chain in the periodic regime is 3.1 times cheaper. The full run to $t = 10.5$ s is accelerated less, by a factor of 2.3, because in `solids4foam` the coupling is switched on only at $t = 2$ s and only the flow is computed before that. For the chain, however,

the time step $\Delta t = 10^{-3}$ s, with which all its computations in Sect. 6 were performed, is sufficient (halving it changes the statistics by less than 0.2%, Table 7). The time per step hardly changes, so per second of simulated time the computation with the chain is 6.0 times faster, and the full run to $t = 10.5$ s is 4.5 times faster (1.1 h against 5.0 h). The gain has two causes: the structural solution is practically free, and the coupling iterations are performed within a single PIMPLE loop, whereas in `solids4foam` each coupling iteration involves a full PIMPLE loop and a nonlinear solid solution.

Table 11 FSI2: cost and accuracy of the computations with the rigid-segment chain and with `solids4foam` on the same machine (Intel Core i5-12450H, 2 processes). Deviations are relative to the reference [29]

	Chain, mesh M1		`solids4foam`, 2x mesh
Fluid cells	18 860		21 344
Structure	20 segments		2 520 cells
Coupling per step	6 PIMPLE iterations		IQN-ILS, ≈ 4.6 iterations[1]
Δt, s	10^{-3}	$5 \cdot 10^{-4}$	$5 \cdot 10^{-4}$
Time per step at $t = 8$–10.5 s, s	0.41	0.40	1.24
Time per 1 s of simulated time, min	6.9	13.2	41.3
Total time to $t = 10.5$ s, h	1.1	2.1	5.0
u_y frequency	+1.5%	[2]	+1.8%[1]
u_y amplitude	+2.5%	[2]	−1.3%[1]
Mean drag	+1.3%	[2]	+0.5%[1]
Lift amplitude	+4.8%	[2]	+7.8%[1]

[1]From the verification data of the `solids4foam` developers on the same mesh; each IQN-ILS iteration includes 3 outer PIMPLE iterations.

[2]Halving the time step changes the statistics by less than 0.2% (Table 7).

Choice of N and time step.

The highest frequency of the chain grows as N^2: with $\Delta t = 10^{-3}$ s, $\omega_{\max}\Delta t = 1.1$ at $N = 20$ and 2.7 at $N = 40$ in FSI2; in FSI3 ($\Delta t = 5 \cdot 10^{-4}$ s) it is 3.5 and 8.5. The Newmark scheme with $\gamma = 0.5$, $\beta = 0.25$ remains stable, but these zigzag hinge modes are neither resolved nor damped. If they are excited, they can be suppressed by hinge damping (Sect. 3.4) or by a small numerical dissipation of the scheme ($\gamma = 0.55$, $\beta = (\gamma + \frac{1}{2})^2/4$) without affecting the lowest modes, for which $\omega_1 \Delta t \sim 10^{-2}$. Segments shorter than the thickness ($\Delta x < h$, i.e. $N > 17$ in the benchmark) resolve wavelengths that rod theory does not describe; this does no harm to the lowest modes, but gives no benefit either.

Extensions.

The restriction to the Euler–Bernoulli (Rayleigh) rod is a consequence of the joint type rather than of the rigid-segment idea itself. A composite joint $\{P_y, R_z\}$ with a transverse spring $\kappa GA/\Delta x$ (shear spring–damping elements of this kind are used in

the classical formulation of the RFEM [17, Sect. 3.6]) gives the Timoshenko beam in the limit and would remove the model part of the difference found in Sect. 6.6; a joint $\{P_x, P_y, R_z\}$ with axial, shear and bending springs gives a discrete geometrically exact Reissner rod [8, 9], and spherical joints with two bending springs and one torsional spring give a spatial rod. The joint-space restraint generalises directly to multi-degree-of-freedom joints. Variable stiffness and mass, nonlinear or viscoelastic hinges and active moments (for example, a time-dependent angle $\theta_i^0(t)$ as a model of muscle actuation) require no change of the formulation. In particular, a free hinge between flexible parts, as in the hinged two-beam system of Zhang et al. [7], is obtained by setting the stiffness of one restraint to zero, and an actuated hinge by prescribing $\theta_i^0(t)$.

Limitations.

The model gives bending moments at the hinges rather than a stress field. The library supports only tree-structured systems, so plate networks with closed loops cannot be built directly, although strips with flexibility in one direction are possible. The coupling is partitioned, and its stability at large added-mass ratios is ensured by outer iterations with relaxation of the accelerations, whose factor must decrease as the mass ratio grows.

8 Conclusions

A chain of rigid segments with distributed inertia, belonging to the class of rigid finite element models, has been considered as a model of a slender flexible body for fluid–structure interaction, and three ideas have been substantiated that make it a full-fledged alternative to more complex structural models in FSI.

The first idea is embeddability. The chain is implemented in the standard multibody library of OpenFOAM, the most widely used open-source CFD toolbox, by a single restraint of about 90 lines that applies the hinge moment as a generalised joint force. Everything else is a dictionary of bodies, joints and restraints; the flow solver, mesh motion and multibody integrator are used unchanged.

The second idea is consistency. The mass matrix is obtained in closed form, and the continuum limit leads to the Euler–Bernoulli (Rayleigh) beam, all of whose boundary conditions follow from the limiting problem. Second-order convergence of frequencies and mode shapes is provided by a clamp hinge of stiffness $2EI/\Delta x$; this division is dual to the primary division of the RFEM. The model is more accurate than a second-order finite-difference scheme with the same number of unknowns.

The third idea is geometric nonlinearity at no extra cost. The multibody solver integrates the exact equations of the chain, and its limit is the inextensible geometrically exact rod. Second-order convergence is retained for large deflections, as verified against the elastica up to a tip rotation of 72° and for free oscillations of large amplitude.

In the Turek–Hron benchmark (with the relative deviations defined in Sect. 6.1), the deflections and frequencies in the structural tests differ from the reference by at most 1.6%, and the axial displacements by at most 3.4%. In FSI2 the solution is converged in the fluid mesh, time step and coupling scheme, and the frequencies

exceed the reference by 1.5%; this difference consists of the contributions of the one-dimensional idealisation (the second dry mode of the rod is 1.2% higher than that of the two-dimensional flag) and of the flow computation. In FSI3 the partitioned coupling is stable at an added-mass ratio of about 14, all statistics lie within the range of other solvers, and the frequencies agree with a high-order solution to 0.2%. The rigid-flag tests show that the remaining drag differences are due to the flow discretisation. On the same machine and at comparable accuracy, the FSI2 computation with the chain is 3.1 times faster than with `solids4foam` for the same time step and 6 times faster for the time step sufficient for the chain, and its cost is determined by the flow computation alone. Thus, contrary to a view widespread in FSI, a properly constructed chain of rigid bodies is a consistent second-order discretisation of an elastic rod and, embedded in the multibody solver of a CFD toolbox, provides a cheap and accurate structural model for FSI of slender bodies.

Declarations

Funding. The study was supported by a grant of the Russian Science Foundation (project no. 22-79-10033-П).

Competing interests. The authors declare no competing interests.

Data availability. The data supporting the findings of this study are contained in the article; the raw computational data are available from the corresponding author on reasonable request.

Author contributions. A. Nuriev: Conceptualization, Methodology, Formal analysis, Software, Investigation, Writing – original draft. B. Affane: Methodology, Validation, Investigation, Writing – original draft. A. Pozdeeva: Investigation, Data curation, Validation. All authors read and approved the final manuscript.

Code availability. The restraint `linearJointSpring` and the OpenFOAM case of the Turek–Hron FSI2 and FSI3 tests, with the case generator and the post-processing script, are available at https://github.com/alexandra-pozdeeva/linearJointSpring under the GNU General Public License v3.0.

Appendix A Implementation in OpenFOAM

A.1 Capabilities of the toolbox and the model dictionary

The `rigidBodyDynamics` library describes a tree of rigid bodies connected by joints: revolute, prismatic, spherical, composite and floating. Given the joint coordinates and velocities, the generalised joint forces and the external forces on the bodies, the articulated-body algorithm [27] returns the joint accelerations, including all velocity-dependent terms. Time integration is performed by one of the built-in schemes (Newmark, Crank–Nicolson or symplectic). Restraints are run-time selectable classes chosen by name from the input dictionary. The mesh-motion solver `rigidBodyMotion` integrates the pressure and viscous forces over the patches of each body, applies them to the bodies, moves the patches with the bodies and deforms the interior mesh by

a solver specified in the same dictionary (here, a displacement Laplacian). It can be used with any OpenFOAM solver that supports dynamic meshes, in serial or in parallel with the standard domain decomposition. All computations in this work were performed with OpenFOAM v2112 (ESI); the restraint library and the test cases also run without changes in v2412.

Table A1 relates the model quantities to the entries of the dictionary `constant/dynamicMeshDict`, and Fig. A1 shows a fragment of it for the Turek–Hron flag.

Table A1 Correspondence between the rigid-segment model and the entries of `constant/dynamicMeshDict` (two-dimensional case, per unit width)

Model quantity	Dictionary entry	Value
segment i	`bodies/segment`i, `type` `rigidBody`	
topology	`parent`	segment $i-1$; the support for $i=0$
hinge position	`transform` (offset from the parent origin)	$(\Delta x_{i-1}, 0, 0)$; clamp point for $i=0$
hinge	`joint`, type `Rz`	coordinate $\theta_i = \varphi_i - \varphi_{i-1}$
mass	`mass`	$m_i = \rho A\, \Delta x_i$
centre of mass	`centreOfMass`	$(\Delta x_i/2, 0, 0)$
moment of inertia about c.m.	`inertia`, zz component	$m_i(\Delta x_i^2 + h^2)/12$
wetted surface	`patches`	patch of segment i
hinge stiffness	`restraints/hinge`i: `linearJointSpring`	$k_i = 2EI/(\Delta x_{i-1} + \Delta x_i)$, $\Delta x_{-1} = 0$
hinge damping	`damping`	$c_i = \eta k_i$
time integration	`solver`, type `Newmark`	$\gamma = 0.5$, $\beta = 0.25$
inertia scaling	`accelerationDamping`	1
coupling	`accelerationRelaxation`	see Sect. 6.2

A.2 Joint-space restraint

The standard restraint `linearAxialAngularSpring` applies to a single body the moment $-[k\theta + c\,(\boldsymbol{\omega}\cdot\mathbf{a})]\mathbf{a}$, where θ is the rotation relative to a fixed reference orientation, $\boldsymbol{\omega}$ the absolute angular velocity of this body and $\mathbf{a}$ the axis. Applied to the segments of a chain, it has three drawbacks: it models a beam on an elastic rotational foundation, since the moment is proportional to φ_i rather than to $\varphi_i - \varphi_{i-1}$; it applies no reaction to the parent body, so action and reaction are not balanced; and it damps the absolute rather than the relative rotation, which causes spurious bending when the support itself rotates. Expressing the angle in the parent frame removes only the first of these drawbacks.

The restraint `linearJointSpring` implements the moment (16) as a generalised joint force. The core of its `restrain` method is:

```
const joint& jnt = model_.joints()[bodyIndex_]; // joint of the body to its parent
const label qi = jnt.qIndex(); // its generalised coordinate
const scalar theta = state.q()[qi] - refAngle_;
const scalar thetaDot = state.qDot()[qi];
tau[qi] += -(stiffness_*theta + damping_*thetaDot);
```

```
motionSolverLibs ("librigidBodyMeshMotion.so" "libfvMotionSolvers.so"
                  "librigidBodyDynamicsSpring.so");
motionSolver rigidBodyMotionSolver;
meshSolver { solver displacementLaplacian;
             diffusivity inverseDistance
                 (cylinder segment0Wall ... segment19Wall); }
solver { type Newmark; gamma 0.5; beta 0.25; }
accelerationRelaxation 0.5;
accelerationDamping 1;
bodies
{
    segment0
    {
        type rigidBody;
        parent root; // fixed cylinder
        mass 3.5101; // rho*A*dx
        centreOfMass (0.0087753 0 0); // dx/2
        inertia (0.29263 0 0 0.29260 0 2.0710e-4); // Izz = m(dx^2+h^2)/12
        transform (1 0 0 0 1 0 0 0 1) (0.24899 0.2 0); // clamp point
        joint { type Rz; }
        patches (segment0Wall);
    }
    segment1
    {
        type rigidBody;
        parent segment0;
        mass 3.5101;
        centreOfMass (0.0087753 0 0);
        inertia (0.29263 0 0 0.29260 0 2.0710e-4);
        transform (1 0 0 0 1 0 0 0 1) (0.0175505 0 0); // length of parent
        joint { type Rz; }
        patches (segment1Wall);
    }
    // ... segment2 ... segment19
}
restraints
{
    hinge0 { type linearJointSpring; body segment0;
             stiffness 126.619; damping 0; } // 2EI/dx
    hinge1 { type linearJointSpring; body segment1;
             stiffness 63.309; damping 0; } // EI/dx
    // ... hinge19
}
```

Fig. A1 Fragment of `constant/dynamicMeshDict` for the Turek–Hron flag in FSI2 ($N = 20$, $EI = 1.111\ \mathrm{N\,m^2}$, $\rho A = 200\ \mathrm{kg/m}$, depth 1 m). The components I_{xx}, I_{yy} do not affect planar motion and only keep the inertia tensor positive definite

The class reads `body`, `stiffness`, `damping` and an optional `referenceAngle` θ_i^0, and stops with an error if the joint has more than one degree of freedom. It is compiled with `wmake` into a user library loaded through the `motionSolverLibs` entry; the run-time selection mechanism registers it among the available restraints. A one-line `Make/files` is sufficient for this, and the OpenFOAM source code is not modified.

A.3 Workflow and practical rules

Setting up an FSI computation with a flexible body takes four steps.

1. *Mesh.* Any mesh generator can be used; the only requirement is that the surface of the flexible body is split into one patch per segment and that segment boundaries lie on mesh faces. With `blockMesh`, the flag surface is split by the `topoSet` and `createPatch` utilities.
2. *Dictionary.* The bodies and restraints of Table A1 are written by a short script from L, EI, ρA, h and N, or from a list of segment lengths Δx_i for a non-uniform division.
3. *The restraint library* is compiled once with `wmake`.
4. *Run.* The unmodified flow solver (here `pimpleFoam`) is run with `moveMeshOuterCorrectors` enabled, so that the bodies and the mesh are updated at every outer coupling iteration.

The following rules are easy to violate, and violating them noticeably changes the results.

- The first segment must be a moving body attached to the support by a hinge with $k_0 = 2EI/\Delta x_0$. Fixing it rigidly to the support raises the frequencies by an amount of order $1/N$ (by 11% at $N = 10$), and choosing $k_0 = EI/\Delta x$ lowers them by a similar amount (Table 2). An equivalent alternative is the primary division of the RFEM: a fixed half element at the clamp (part of the stationary wall), hinges $EI/\Delta x$ at the midpoints of the parts and a half-length end element.
- The solver parameter `accelerationDamping` must equal 1. A value $\alpha < 1$ scales the computed accelerations, which is equivalent to multiplying all inertias by $1/\alpha$, and the frequencies are multiplied by $\sqrt{\alpha}$ (by -2.5% for $\alpha = 0.95$). Values below 1 are intended for steady computations.
- The inertia of each segment must include the rotary inertia of the cross-section $m_i h^2/12$, which is comparable with $m_i \Delta x_i^2/12$ for $\Delta x_i \sim h$. For two-dimensional bodies the plane-strain stiffness $E/(1-\nu^2)$ should be used.
- The mesh motion should use the diffusivity $1/r$ (`inverseDistance`). The sharper distribution $1/r^2$ (`quadratic inverseDistance`) concentrated the deformation in a few cells between differently rotating segments and destroyed the mesh at large amplitudes in FSI2.
- The relaxation factor of the accelerations in the outer iterations must satisfy the estimate $\omega \lesssim 2/(1 + m_a/m)$, where m_a/m is the ratio of the added mass to the body mass.
- The highest frequency of the chain grows as N^2; the Newmark scheme is unconditionally stable, but unresolved high modes may need damping (Sects. 3.4 and 7).

References

[1] Tuković, Ž., Karač, A., Cardiff, P., Jasak, H., Ivanković, A.: OpenFOAM finite volume solver for fluid-solid interaction. Transactions of FAMENA **42**(3), 1–31 (2018) https://doi.org/10.21278/TOF.42301

[2] Cardiff, P., Batistić, I., Tuković, Ž.: solids4foam: A toolbox for performing solid mechanics and fluid-solid interaction simulations in OpenFOAM. Journal of Open

Source Software **10**(108), 7407 (2025) https://doi.org/10.21105/joss.07407

[3] Chourdakis, G., Davis, K., Rodenberg, B., Schulte, M., Simonis, F., Uekermann, B., *et al.*: preCICE v2: A sustainable and user-friendly coupling library. Open Research Europe **2**, 51 (2022)

[4] Masarati, P., Morandini, M., Mantegazza, P.: An efficient formulation for general-purpose multibody/multiphysics analysis. Journal of Computational and Nonlinear Dynamics **9**(4), 041001 (2014)

[5] Liu, Y., Xiao, Q.: Development of a fully coupled aero-hydro-mooring-elastic tool for floating offshore wind turbines. In: Proceedings of the 13th OpenFOAM Workshop, Shanghai, China, pp. 354–357 (2018)

[6] Joshi, V., Jaiman, R.K., Ollivier-Gooch, C.: A variational flexible multibody formulation for partitioned fluid–structure interaction: Application to bat-inspired drones and unmanned air-vehicles. Computers & Mathematics with Applications **80**, 2707–2737 (2020)

[7] Zhang, Z., Yang, Z., Golubev, V., Liu, L., Chen, G.: Numerical simulation method for fluid–structure interaction of deformable structures based on multibody dynamics. Aerospace **13**, 691 (2026) https://doi.org/10.3390/aerospace13080691

[8] Reissner, E.: On one-dimensional finite-strain beam theory: The plane problem. Zeitschrift für angewandte Mathematik und Physik (ZAMP) **23**, 795–804 (1972) https://doi.org/10.1007/BF01602645

[9] Simo, J.C.: A finite strain beam formulation. The three-dimensional dynamic problem. Part I. Computer Methods in Applied Mechanics and Engineering **49**, 55–70 (1985)

[10] Lang, H., Linn, J., Arnold, M.: Multi-body dynamics simulation of geometrically exact Cosserat rods. Multibody System Dynamics **25**, 285–312 (2011)

[11] Bergou, M., Wardetzky, M., Robinson, S., Audoly, B., Grinspun, E.: Discrete elastic rods. ACM Transactions on Graphics **27**(3), 63 (2008)

[12] Shabana, A.A.: Flexible multibody dynamics: Review of past and recent developments. Multibody System Dynamics **1**, 189–222 (1997) https://doi.org/10.1023/A:1009745432698

[13] Hencky, H.: Über die angenäherte Lösung von Stabilitätsproblemen im Raum mittels der elastischen Gelenkkette. Der Eisenbau **11**, 437–452 (1920)

[14] Wang, C.M., Zhang, H., Gao, R.P., Duan, W.H., Challamel, N.: Hencky bar-chain model for buckling and vibration of beams with elastic end restraints. International Journal of Structural Stability and Dynamics **15**(7), 1540007 (2015)

https://doi.org/10.1142/S0219455415400076

[15] Wang, C.M., Zhang, H., Challamel, N., Pan, W.H.: Hencky Bar-Chain/Net for Structural Analysis. World Scientific, London (2020). https://doi.org/10.1142/q0237

[16] Kruszewski, J., Gawroński, W., Wittbrodt, E., Najbar, F., Grabowski, S.: Metoda Sztywnych Elementów Skończonych (The Rigid Finite Element Method). Arkady, Warszawa (1975)

[17] Wittbrodt, E., Adamiec-Wójcik, I., Wojciech, S.: Dynamics of Flexible Multibody Systems: Rigid Finite Element Method. Foundations of Engineering Mechanics. Springer, Berlin, Heidelberg (2006). https://doi.org/10.1007/978-3-540-32352-5

[18] Szczotka, M.: A modification of the rigid finite element method and its application to the J-lay problem. Acta Mechanica **220**(1), 183–198 (2011) https://doi.org/10.1007/s00707-011-0470-6

[19] Howell, L.L., Midha, A.: Parametric deflection approximations for end-loaded, large-deflection beams in compliant mechanisms. Journal of Mechanical Design **117**(1), 156–165 (1995) https://doi.org/10.1115/1.2826101

[20] Yu, Y.-Q., Li, Q., Xu, Q.-P.: Pseudo-rigid-body dynamic modeling and analysis of compliant mechanisms. Proceedings of the Institution of Mechanical Engineers, Part C: Journal of Mechanical Engineering Science **232**(9), 1665–1678 (2018) https://doi.org/10.1177/0954406217707547

[21] Neubert, V.H., Lee, H.: Lumped parameter beam models based on mechanical impedance. Interim Report 6 (DTIC AD0810815), Department of Engineering Mechanics, The Pennsylvania State University (1967)

[22] Rangaiah, V.P., Neubert, V.H.: Finite element for Timoshenko beam based on mechanical impedance. Progress Report 1 (DTIC AD0724332), Department of Engineering Mechanics, The Pennsylvania State University (1971)

[23] Eldredge, J.D., Toomey, J., Medina, A.: On the roles of chord-wise flexibility in a flapping wing with hovering kinematics. Journal of Fluid Mechanics **659**, 94–115 (2010) https://doi.org/10.1017/S0022112010002363

[24] Le, V.D.T., Nguyen, A.T., Dang, N.T.: Multibody-dynamics approach to study the deformation and aerodynamics of an insect wing. AIAA Journal **61**, 2500–2516 (2023)

[25] Li, R., Xiao, Q., Liu, Y., Hu, J., Li, L., Li, G., Liu, H., Hu, K., Wen, L.: A multi-body dynamics based numerical modelling tool for solving aquatic biomimetic problems. Bioinspiration & Biomimetics **13**, 056001 (2018)

[26] Arranz, G., Martínez-Muriel, C., Flores, O., García-Villalba, M.: Fluid–structure interaction of multi-body systems: Methodology and applications. Journal of Fluids and Structures **110**, 103519 (2022) https://doi.org/10.1016/j.jfluidstructs.2022.103519

[27] Featherstone, R.: Rigid Body Dynamics Algorithms. Springer, New York (2008)

[28] Turek, S., Hron, J.: Proposal for numerical benchmarking of fluid-structure interaction between an elastic object and laminar incompressible flow. In: Bungartz, H.-J., Schäfer, M. (eds.) Fluid-Structure Interaction: Modelling, Simulation, Optimisation. Lecture Notes in Computational Science and Engineering, vol. 53, pp. 371–385. Springer, Berlin, Heidelberg (2006)

[29] Turek, S., Hron, J., Mádlík, M., Razzaq, M., Wobker, H., Acker, J.F.: Numerical simulation and benchmarking of a monolithic multigrid solver for fluid–structure interaction problems with application to hemodynamics. In: Bungartz, H.-J., Mehl, M., Schäfer, M. (eds.) Fluid Structure Interaction II. Lecture Notes in Computational Science and Engineering, vol. 73, pp. 193–220. Springer, Berlin, Heidelberg (2010). https://doi.org/10.1007/978-3-642-14206-2_8

[30] Liu, J.: A second-order stable explicit interface advancing scheme for FSI with both rigid and elastic structures and its application to fish swimming simulations. Computers & Fluids (2015) https://doi.org/10.1016/j.compfluid.2015.06.002

[31] Jasak, H., Tuković, Ž.: Automatic mesh motion for the unstructured finite volume method. Transactions of FAMENA **30**(2), 1–20 (2006)

[32] Causin, P., Gerbeau, J.-F., Nobile, F.: Added-mass effect in the design of partitioned algorithms for fluid–structure problems. Computer Methods in Applied Mechanics and Engineering **194**(42–44), 4506–4527 (2005)

[33] Förster, C., Wall, W.A., Ramm, E.: Artificial added mass instabilities in sequential staggered coupling of nonlinear structures and incompressible viscous flows. Computer Methods in Applied Mechanics and Engineering **196**(7), 1278–1293 (2007) https://doi.org/10.1016/j.cma.2006.09.002

[34] Küttler, U., Wall, W.A.: Fixed-point fluid–structure interaction solvers with dynamic relaxation. Computational Mechanics **43**, 61–72 (2008) https://doi.org/10.1007/s00466-008-0255-5

[35] Tian, F.-B., Dai, H., Luo, H., Doyle, J.F., Rousseau, B.: Fluid–structure interaction involving large deformations: 3D simulations and applications to biological systems. Journal of Computational Physics **258**, 451–469 (2014) https://doi.org/10.1016/j.jcp.2013.10.047

[36] Turek, S., Hron, J., Razzaq, M., Wobker, H., Schäfer, M.: Numerical benchmarking of fluid–structure interaction: A comparison of different discretization

and solution approaches. In: Bungartz, H.-J., Mehl, M., Schäfer, M. (eds.) Fluid Structure Interaction II. Lecture Notes in Computational Science and Engineering, vol. 73, pp. 413–424. Springer, Berlin, Heidelberg (2010). https://doi.org/10.1007/978-3-642-14206-2_15

[37] Lozovskiy, A., Olshanskii, M.A., Salamatova, V., Vassilevski, Y.V.: An unconditionally stable semi-implicit FSI finite element method. Computer Methods in Applied Mechanics and Engineering **297**, 437–454 (2015) https://doi.org/10.1016/j.cma.2015.09.014

[38] Degroote, J., Haelterman, R., Annerel, S., Bruggeman, P., Vierendeels, J.: Performance of partitioned procedures in fluid–structure interaction. Computers & Structures **88**(7–8), 446–457 (2010) https://doi.org/10.1016/j.compstruc.2009.12.006